Journal of
*Marine Science and Engineering*

MDPI

*Article*

# Effect of Hydrate Saturation on Permeability Anisotropy for Hydrate-Bearing Turbidite Sediments Based on Pore-Scale Seepage Simulation

**Ruirui Li [1,2], Zhenhua Han [1,2,*], Luqing Zhang [1,2], Jian Zhou [3] and Song Wang [1,2]**

[1] Key Laboratory of Shale Gas and Geoengineering, Institute of Geology and Geophysics, Chinese Academy of Sciences, Beijing 100029, China
[2] Innovation Academy for Earth Science, CAS, Beijing 100029, China
[3] Key Laboratory of Urban Security and Disaster Engineering of Ministry of Education, Beijing University of Technology, Beijing 100124, China
* Correspondence: hanzhenhua@mail.iggcas.ac.cn

**Abstract:** The permeability of natural gas hydrate (NGH) turbidite reservoirs typically exhibits significant anisotropy, with anisotropy being a crucial basis for evaluating reservoir production. The presence of hydrates, as a crucial constituent of the solid framework, not only impacts the overall permeability but also influences the permeability anisotropy. To investigate the saturation sensitivity of permeability anisotropy, a series of simulations are performed by integrating particle flow and computational fluid dynamics methods to construct the homogeneous and layered numerical samples and compute the evolution of permeability anisotropy. It is shown that the permeability is isotropic for homogeneous sediments and the isotropy remains unchanged regardless of variations in hydrate saturation. The permeability of layered sediments, in contrast, exhibits significant anisotropy due to the presence of dominant channels within the coarse layer. For uniformly distributed hydrates, the more effective blockage in coarse layers results in a reduction in anisotropy. While for preferentially distributed hydrates, the excess blocking of coarse layers makes the dominant channels transfer to the fine layers, the further blocking causes a U-shaped anisotropy–saturation curve characterized by a decrease–increase transformation. During the reservoir production process, the preponderance channels blocked by hydrates will be cleared and the horizontal permeability will significantly increase. As a result, the production efficiency of horizontal wells may exceed expectations. The findings offer a parameter support for production estimation and environmental assessment.

**Keywords:** natural gas hydrate; hydrate saturation; permeability; anisotropy; computational fluid dynamics

check for updates

**Citation:** Li, R.; Han, Z.; Zhang, L.; Zhou, J.; Wang, S. Effect of Hydrate Saturation on Permeability Anisotropy for Hydrate-Bearing Turbidite Sediments Based on Pore-Scale Seepage Simulation. *J. Mar. Sci. Eng.* **2024**, *12*, 1079. https://doi.org/10.3390/jmse12071079

Academic Editor: Dejan Brkić

Received: 20 May 2024
Revised: 21 June 2024
Accepted: 21 June 2024
Published: 26 June 2024

**Copyright:** © 2024 by the authors. Licensee MDPI, Basel, Switzerland. This article is an open access article distributed under the terms and conditions of the Creative Commons Attribution (CC BY) license (https://creativecommons.org/licenses/by/4.0/).

## 1. Introduction

Natural gas hydrate (NGH) is an ice-like solid compound, primarily found in marine turbidite sediments and beneath permafrost [1–4]. The global abundance of natural gas hydrates makes them of interest for the global and oceanic carbon cycle [5–8] and has made NGH an especially high-interest target as a potential future source of energy [9–14]. Moreover, their utilization may have far-reaching implications for the global energy landscape, climate change mitigation and prevention of natural hazards [11,13,15,16]. The extraction of hydrates involves a multitude of intricate processes, including phase transition, mass and heat transfer, reservoir deformation, as well as multiphase seepage [17]. Among them, the seepage characteristic, quantified by the permeability, determines the efficiency of hydrate extraction and the stability of reservoir [18–20]. Naturally, permeability is determined by the microscopic pore structure of target reservoir [20]. Both the oriented particle arrangement in micro scale and the bedding structure in macro scale will cause the inherent anisotropy of permeability [21,22]. Moreover, with the change of the NGH saturation, the

permeability and anisotropy will change radically, which brings great uncertainty to the evaluation of engineering and environmental effects during NGH exploitation [21–24]. In practice, the relatively high permeability in the horizontal direction (parallel to the bedding plane) facilitates the efficient horizontal gas transportation, thereby enhancing long-term gas production from horizontal wells [25–27]. Therefore, it is important to have a deep understanding of the influence of hydrate saturation on permeability anisotropy.

Naturally, the abrupt variation in particle size is the most prominent characteristic of marine turbidite sediments [28,29]. Due to the periodic occurrence of turbidity currents, the coarse-grained layers from turbidity currents are often interbedded with fine-grained hemipelagic and pelagic facies sediment layers [30–34]. For example, the hydrate-bearing turbidite sediments in northern Cascadia exhibit a prominent feature of abundant sand layers, measuring several centimeters in thickness, which are interspersed among clay and silty layers [28]. The turbidite reservoir in the Eastern Nankai Trough Area comprises multiple sand layers, each approximately 1 cm thick [35]. Additionally, the hydrate reservoirs in Ulleung Basin (located on the east side of the Korean peninsula), Shenhu area (situated in the South China sea) and northern Gulf of Mexico exhibit analogous characteristics [36–38]. The abrupt variation in particle size results in the formation of beddings [31,39], subsequently leading to the inherent permeability anisotropy [40]. It has been shown that the horizontal permeability can be twice as large as the vertical permeability for turbidite sediments [22]. Moreover, the occurrence of hydrates also has a particle size correlation [41]. According to the observation in the Integrated Ocean Drilling Program, the sand layers in drill cores demonstrate a significant cooling phenomenon; the reverse is the case in clay and silty layers, indicating that the coarse-grained layers have higher hydrate saturation [28].

Naturally, hydrates, which occupy part of the pore space and participate in the forming of solid skeletons, further affect the pore structure and permeability [42]. With the evolution of temperature and pressure environments, the decomposition and secondary synthesis of hydrates leads to significant changes in saturation, becoming one of the secondary factors that impact the permeability anisotropy [43,44]. The pore habits of hydrates in natural reservoirs have been demonstrated to be diverse and intricate, encompassing grain coating, pore filling, cementation and load bearing [20,45]. Based on the pore structure, a series of theoretical models, like the parallel capillary model, Kozeny grain model and University of Tokyo model, have been proposed to describe the permeability–saturation relationship [46–49]. In these models, the reservoir sediments are simplified into uniformly distributed isotropic materials to analyze the effects of hydrate pore habits and saturation on permeability. However, the inherent permeability anisotropy and its evolution with changing saturation are often ignored. A few studies have observed the anisotropy of permeability in hydrate-bearing sediments, yet they have not taken into account the combined effects of primary sedimentary structure and secondary hydrate disturbance [44,50]. Moreover, the profound exploration of the evolution mechanism of anisotropy remains challenging due to the limitations of conventional experimental and numerical methods [44,51].

Based on the geological background of the turbidite reservoir in northern Cascadia, this work explores the saturation sensitivity of permeability anisotropy. A practical method for hydrate generation and saturation determination is developed and a series of simulations are performed by integrating particle flow and computational fluid dynamics methods to construct the numerical samples and compute the permeability anisotropy. Based on the homogeneous and layered sediment models, the evolution of permeability anisotropy under different geological backgrounds are revealed and the microscopic mechanisms are discussed. Related findings can provide basic parameters for hydrate development.

## 2. Modelling Methodology and Scenarios

### *2.1. Pore-Scale Modeling for Hydrate-Bearing Sediment*

Theoretically, permeability is defined as the fluid-passing ability under a certain pressure gradient [20]. The numerical determination of permeability requires the simulation of the fluid transport process in a pore system. Since single-phase flow in a sediment porous

medium takes solid particles as the geometric boundaries, modeling sediment particles is the initial step for permeability evaluation. To restore the in situ packing structure and characterize the primary anisotropy, the pluviation method is employed to construct the sediment models, which releases the sediment particles at a certain height to simulate the process of natural deposition. This method enables the simulation of particle deposition in a quiescent water environment, thereby enhancing the fidelity of obtained samples to their in situ counterparts in terms of physical and mechanical properties [52,53]. As demonstrated in our preliminary study, particle flow simulation (PFC) can be applied to numerically simulate the physical process of the pluviation method and construct related pore-scale sediments models [21]. In this discrete element framework, the sediment particles are approximated as spherical balls with the same volume, which are released from a specific height to generate the sediment models [21]. Forces and moments are generated upon contact between particles [54,55] with the mechanical parameters shown in Table 1 [56,57]. After particle generation, the locations and sizes of all particles are recorded and outputted. An interface tool, COMSOL Multiphysics with MATLAB, is utilized to construct 3D geometric models with the outputted particle information (Figure 1).

**Table 1.** Parameters in numerical simulation.

| Parameter | Value |
|---|---|
| Sediment density (kg/m$^3$) | 1600 |
| Normal stiffness $k_n$ (N/m) | $1.5 \times 10^9$ |
| Shear stiffness $k_s$ (N/m) | $1.0 \times 10^9$ |
| Friction coefficient $\mu$ | 0.2 |
| Normal critical damping ratio $\beta_n$ | 1.0 |
| Shear critical damping ratio $\beta_s$ | 0 |
| Fluid density (kg/m$^3$) | 1000 |
| Dynamic viscosity (Pa·s) | 0.001 |

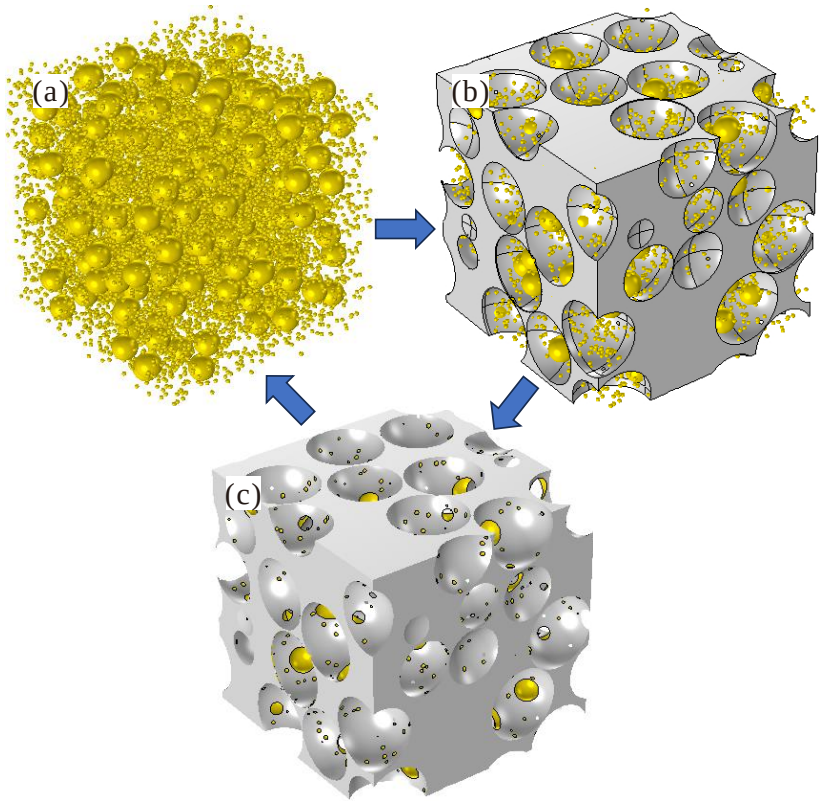



**Figure 1.** Pore geometry model of hydrate-bearing sediments: (**a**) hydrate particles; (**b**) primary pore model; and (**c**) hydrate-bearing pore model.

Naturally, hydrates occupy part of the reservoir pore space and participate in the forming of a solid skeleton. Morphologically, hydrates exhibit various pore habits and can either adhere to sediment particle surfaces (grain coating) or fill pore centers (pore filling). However, the sediment particles and hydrate particles are typically segregated in conventional DEM simulations, resulting in an exclusive pore habit of pore-filling [58–60]. This strategy is convenient for saturation calculation, but the obtained model deviates significantly from the actual pore habits. The hydrate generation in this study employs a stochastic approach, enabling the hydrates to spatially coincide with the sediments. In this manner, the distribution of hydrate particles is more closely aligned with the actual situation. However, the direct calculation of hydrate saturation is not feasible when dealing with the overlapped particles, primarily due to the unknown overlap volume between hydrates and sediments. Technically, a Boolean operation is employed to crop hydrate particles from the primary pore models, thereby obtaining the actual occupied volume of hydrates (see Figure 1b,c). The process of hydrate formation is divided into multiple sequential steps to approximate the specified saturation. For a saturation $S_{h0}$, the expected volume of hydrate is

$$V_h = VpS_{h0} \tag{1}$$

where $V$ is model volume; $p$ is porosity.

At the first time of hydrate formation, the total volume of hydrate particles is set as $S_{h0}$. After formation, a Boolean operation is employed to crop the hydrate particles. The actual volume of hydrates occupying the pore space, denoted as $V_{h1}$, can be calculated based on the reduction in pore volume after cropping. Due to potential overlap between sediments and hydrates, there will always exist an overlapping volume, resulting in $V_h > V_{h1}$. Accordingly, the volume of hydrate formation at the second time is set as the insufficient value of the first-time hydrate formation:

$$V_2 = V_h - V_{h1} \tag{2}$$

The actual volume of hydrate after the second time of hydrate formation will still experience a certain shortfall due to the overlap. The aforementioned steps are subsequently repeated to approach the specified hydrate saturation $S_{h0}$.

### 2.2. Scenarios

The primary objective of this study is to investigate the impact of hydrate saturation on permeability and permeability anisotropy. Two scenarios with different sedimentary structures are designed as follows:

(1) Homogeneous sediments

The overall permeability response to hydrate saturation is investigated by constructing pore-scale models with homogeneous sediment particles. At first, sediment models are constructed within a cubic domain measuring 100 μm on each side. The sediment particles are uniform in size with a diameter of 9 μm. Afterwards, a smaller cube (30 μm) is positioned at the center of the model, and the sediment particles within the smaller cube are selectively utilized to further construct the pore model in order to mitigate any potential boundary effects. Hydrate particles, with diameters of 3 μm and 0.5 μm for cluster hydrate and dispersed hydrate, respectively [48], are generated to build hydrate-bearing pore models. With the above sequential hydrate formation strategy, 3D hydrate-bearing pore models with saturations of 0, 0.1, 0.2, 0.3 and 0.4 are obtained (see Figure 1).

(2) Layered sediments

The bedding structures in turbidite reservoirs could induce primary anisotropy. And the occurrence of hydrates also demonstrates a notable correlation with bedding, thereby changing the permeability anisotropy. To investigate the impact mechanism of hydrate saturation on permeability anisotropy, layered sediment models are constructed based on the grading of the turbidite NGH reservoir in Northern Cascadia (Figure 2). Particles

with a size smaller than 4 μm and larger than 200 μm are ignored for computational efficiency. The mean particle sizes of the sand layer (coarse layer) and silty clay layer (fine layer) are 64.2 μm and 10.5 μm, respectively. For the coarse–fine binary structure in this reservoir, a 2-layer model is sufficient to reflect the evolution of macroscopic permeability. The size of the layered sediment models is set as 1200 μm, significantly exceeding that of homogeneous sediment models, in order to achieve the representative elementary volume (REV). The particle number in scenario 2 exceeds that of scenario 1 by more than a hundredfold. The three-dimensional solution of computational fluid dynamics requires excessive computational resources due to the larger model size, which is not feasible with current hardware capabilities. Therefore, two-dimensional cross-sections of corresponding 3D models are used for CFD simulation. Four equally spaced cross-sections are extracted for every 3D model and the consistency of the simulation results of the four sections will prove the representativeness.

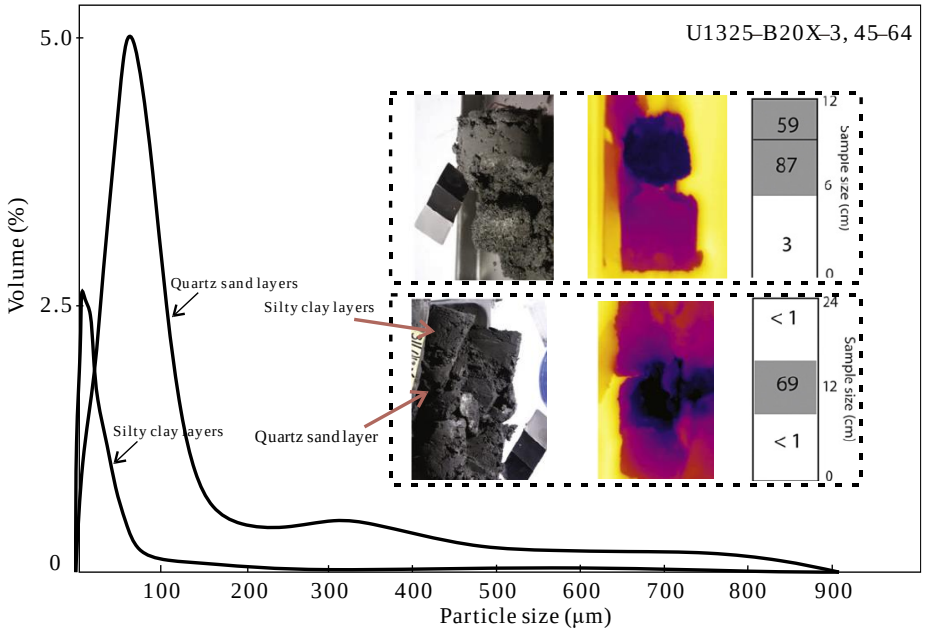



**Figure 2.** Particle size distribution and preferential occurrence of hydrates in Northern Cascadia hydrate reservoir [28].

According to the in situ observation results, hydrates are often found in coarse layers with a saturation ranging from 28% to 87%, while there is almost no hydrate distribution in the adjacent fine particle layers (see Figure 2) [28]. To investigate the effect of hydrate distribution, 2 typical hydrate distribution modes are set. The first mode represents an ideal scenario where hydrates are uniformly and randomly distributed in both the fine and coarse layers (Figure 3). In contrast, the second mode closely resembles the actual characteristics of hydrate distribution, with hydrates preferentially distributed in the coarse layer (Figure 4). All the hydrate particles are uniformly distributed in the coarse layer with the size ranging from 5 μm to 15 μm. The hydrate generation in this study enables the hydrates to spatially coincide with the sediments and a Boolean operation is employed to crop hydrate particles from the primary pore models, thereby obtaining the actual occupied volume of hydrates. With the sequential hydrate formation strategy mentioned in Section 2.1, 2D hydrate-bearing pore models with an overall saturation of 0.025, 0.050, 0.075, 0.100, 0.125, 0.150, 0.175 and 0.200 are obtained. Note that for models with hydrates preferentially distributed in the coarse layer, the local hydrate saturations are 2 times the overall saturations (0.05, 0.10, 0.15, 0.20, 0.25, 0.30, 0.35, 0.40).

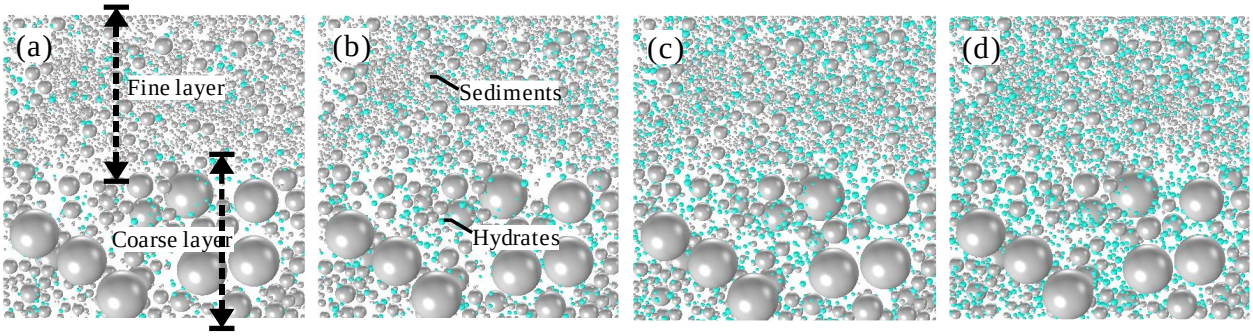



**Figure 3.** Uniformly distributed hydrates in the numerical sample: (**a**) $S_h$ = 0.05; (**b**) $S_h$ = 0.10; (**c**) $S_h$ = 0.15; and (**d**) $S_h$ = 0.20.

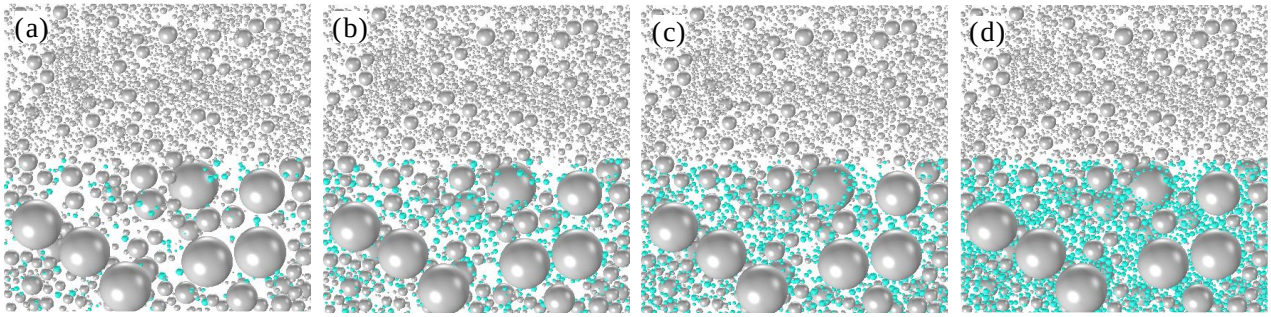



**Figure 4.** Hydrates distributed in coarse layer: (**a**) $S_h$ = 0.050; (**b**) $S_h$ = 0.075; (**c**) $S_h$ = 0.125; and (**d**) $S_h$ = 0.200.

### *2.3. CFD Simulation Methodology*

After model construction, a CFD simulation is applied to reproduce the pore fluid transport characteristics. Based on the momentum conservation and mass conservation, the motion of fluid could be governed by the Navier–Stokes equation as

$$\begin{aligned} &\rho\tfrac{\partial \mathbf{u}}{\partial t} + \rho(\mathbf{u}\cdot\nabla)\mathbf{u} = \nabla\cdot(-p\mathbf{I}+\mathbf{K}) + \mathbf{F} \\ &\rho\nabla\cdot\mathbf{u} = 0 \end{aligned} \tag{3}$$

where $\rho$ is fluid density; $\mathbf{u}$ is velocity vector; $p$ is pressure; $\mathbf{I}$ is identity matrix; $\mathbf{K}$ is viscous stress tensor; and $\mathbf{F}$ is the volume force vector.

For an uncompressible Newtonian fluid, the viscous stress tensor $\mathbf{K}$ can be deduced as

$$\mathbf{K} = \mu(\nabla\mathbf{u} + (\nabla\mathbf{u})^T) \tag{4}$$

where $\mu$ is dynamic viscosity.

In the micro-mesoscopic pore space, the creeping flow exhibits low Reynolds number characteristics ($Re << 1$), resulting in significantly higher viscous stress compared to inertial stress and volume force [57]. Therefore, Equation (3) can be simplified to the Stokes equations as

$$\begin{aligned} &\rho\tfrac{\partial \mathbf{u}}{\partial t} = \nabla\cdot(-p\mathbf{I}+\mathbf{K}) \\ &\rho\nabla\cdot\mathbf{u} = 0 \end{aligned} \tag{5}$$

Steady flow is required for permeability evaluation, therefore, the partial derivative of velocity $\mathbf{u}$ versus time $t$ should be 0 as [57]

$$\begin{aligned} &\nabla\cdot(-p\mathbf{I}+\mathbf{K}) = 0 \\ &\rho\nabla\cdot\mathbf{u} = 0 \end{aligned} \tag{6}$$

Based on the finite element method, COMSOL Multiphysics is used for the model solution. Free tetrahedral meshes and triangle/quadrangle meshes are used to discretize the 3D and 2D geometries, respectively. A grid independence check is conducted to ensures the repeatability of the calculation.

In the direction of flow, the top and bottom boundaries are designated as inflow and outflow boundaries with a constant pressure $P_{in}$ and $P_{out}$, while the four sides and all particle surfaces are defined as walls with zero flow velocity and no slip. Water is selected as the test fluid with relevant parameters detailed in Table 1. The total flows through the models are calculated by boundary integral to obtain the outlet velocity $U_{out}$. The permeability is determined using Darcy's law as follows:

$$k = \frac{U_{out}\mu L}{P_{in} - P_{out}} \tag{7}$$

where $L$ is the model length in the direction of the pressure gradient.

## 3. Results

### 3.1. Effect of Hydrate Saturation on Permeability of Homogeneous Sediments

According to the simulation results, the permeability of homogeneous sediments exhibits minimal anisotropy. When $S_h$ = 0, the horizontal and vertical permeabilities are 84.33 mD and 81.45 mD, respectively. As the saturation increases from 0 to 0.4, the reduction of permeability can reach two orders of magnitude. The horizontal permeability decreases to 7.17 mD (decrease of 92%) and the vertical permeability decreases to 0.90 mD (decrease of 99%). Moreover, the reduction of permeability is rapid in the low-saturation range but becomes slower in the high-saturation range, indicating that even a small quantity of hydrate can significantly alter the permeability. Within the saturation range from 0 to 0.1, the reductions in horizontal and vertical permeabilities are 69% and 68%, respectively, while within the saturation range from 0.1 to 0.4, the reductions in horizontal and vertical permeabilities are only 23% and 31%, respectively. The reduction rates of horizontal and vertical permeabilities are essentially the same within a saturation range of 0–0.3, but become asynchronous at higher saturation levels. As a result, the permeability anisotropy ratio, defined as the ratio of horizontal and vertical permeability ($Pr$), exhibits a segmented evolutionary characteristic. The anisotropy slightly increases from 1.04 to 1.47 within the saturation range of 0–0.3, while it sharply increases from 1.47 to 8.01 within the saturation range of 0.3–0.4 (Figure 5).

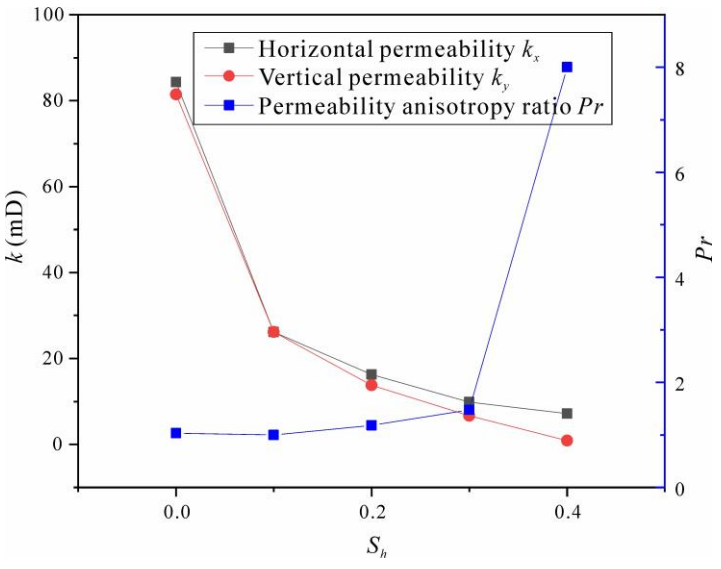



**Figure 5.** Permeability and anisotropy evolution with hydrate saturation in homogeneous model.

For comparison, the permeabilities under different saturations are normalized by the permeability when $S_h = 0$ (Figure 6). The analytical solutions for permeability–saturation relationships in the presence of grain coating (where hydrate preferentially exists on particle surfaces) and pore filling (where hydrate preferentially exists within pore spaces) hydrates in a parallel cylindrical capillary are theoretically derived [46]:

$$k_{GC} = (1 - S_h)^2 \tag{8}$$

$$k_{PF} = 1 - S_h^2 + \frac{2(1 - S_h)^2}{\ln(S_h)} \tag{9}$$

where $k_{GC}$ and $k_{PF}$ are the permeability of capillary with grain coating and pore filling hydrate, respectively.

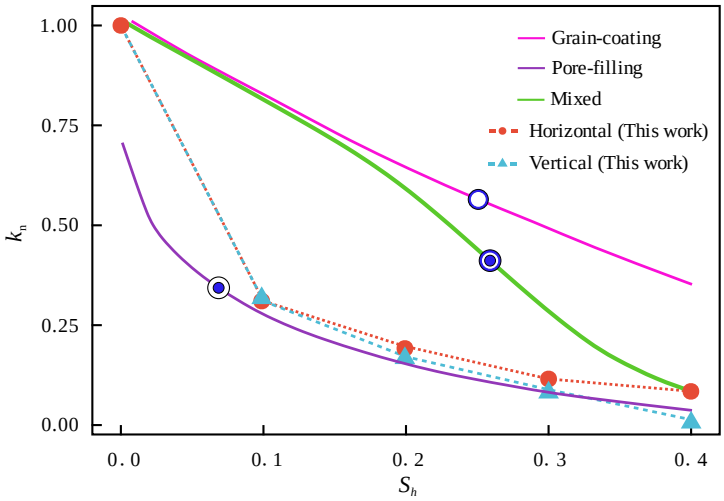



**Figure 6.** Simulated results and theoretical models of normalized permeability.

In addition, by considering the combined impact of these two hydrate growth patterns, a mixed permeability–saturation relationship (where hydrate is present on both particle surfaces and within pore spaces) can be inferred:

$$k_n = (k_{GC})^{1/[1+(S_h/\alpha)^\beta]} \cdot (k_{PF})^{1-1/[1+(S_h/\alpha)^\beta]} \tag{10}$$

where $\alpha$ and $\beta$ are empirical coefficients.

According to the simulation results, the permeability in a specified saturation is generally higher than the analytical solution of pore-filling hydrate and lower than that of grain-coating hydrate, indicating that the proposed hydrate formation strategy is more closely aligned with the actual mixed hydrate distribution. Because the hydrate particles are spherical, even for hydrate particles that are overlapped with sediment particles, their influence on the flow field also has the characteristics of pore-filling mode. Therefore, the overall permeability–saturation relationship is closer to the analytical solution of pore-filling hydrate, especially in the high saturation range.

With increasing hydrate saturation, the pore space is occupied with hydrates and the fluid transport is restricted. Conceptually, hydrates with overlap are considered to be grain-coating mode while hydrates without overlap are considered to be pore-filling mode (Figure 7). The presence of pore-filling hydrates significantly disrupts the flow field, resulting in the bifurcation of seepage channels and leading to a substantial decrease in channel velocity across several orders of magnitude. The grain-coating hydrates, in contrast, only result in the narrowing of flow channels, and the decrease in flow rate is not as significant as that caused by pore-filling hydrates (Figure 7d,e). Moreover, with the increasing in hydrate saturation, hydrates with different pore habits will be connected to each other, thereby

forming cluster and patchy hydrates and locking the seepage channels completely. At high saturation conditions ($S_h \geq 0.3$), more than 70% seepage channels are effectively blocked, leading to great heterogeneity of the pore model and further causing the generation and enhancement of anisotropy. It has been proved that the inhomogeneous distribution of hydrates would cause secondary anisotropy of the pore system [43]. However, in this research, the uniformly distributed hydrates also cause permeability anisotropy in relatively high saturation ranges ($S_h \geq 0.3$). It is considered that the model size limits the representativeness of simulation results within a relatively high saturation range. Only a few seepage channels remain connected in the model in this situation, necessitating an increase in the REV size. Therefore, the confirmation of the increase in anisotropy needs to be further substantiated by considering the scale effect. In general, the scale effect only disturbs the simulation results within a relatively high saturation range. Within this saturation range, the permeability decreases by several orders of magnitude and the disturbance of scale effect is insignificant to the overall evolution of permeability (Figure 6). Therefore, while the accidental increase in anisotropy may be subject to debate, the permeability evolution derived from simulation results remains reliable.

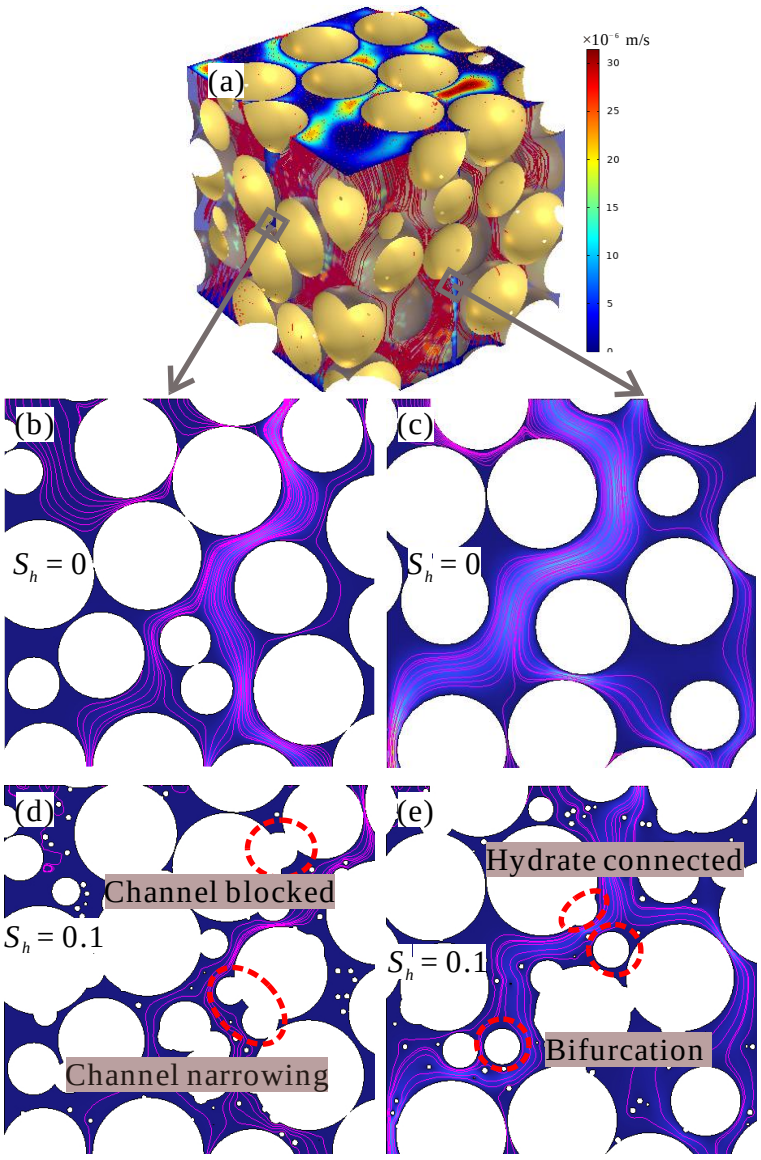



**Figure 7.** Seepage field evolution with increasing hydrate saturation: (**a**) Seepage field; (**b**) Section 1, $S_h$ = 0; (**c**) Section 2, $S_h$ = 0; (**d**) Section 1, $S_h$ = 0.1; and (**e**) Section 2, $S_h$ = 0.1.

### 3.2. Effect of Hydrate Saturation on Permeability of Layered Sediments

#### 3.2.1. Effect of Uniformly Distributed Hydrates

The permeability of layered sediments exhibits significant anisotropy according to the simulation results (Figure 8). When $S_h$ = 0, the horizontal permeability (parallel to the bedding plane, $k_h$) is 86.06 mD, while the vertical permeability (perpendicular to the bedding plane, $k_v$) is 31.16 mD. The permeability anisotropy ratio $Pr$ is 2.76, indicating that the bedding structure could induce significant anisotropy. For uniformly distributed hydrates, both horizontal and vertical permeability continue to decline with saturation increases. Moreover, the permeability and saturation exhibit a quadratic function relationship. As the saturation increases from 0 to 0.2, the horizontal permeability decreases from 86.06 mD to 14.15 mD, while the vertical permeability decreases from 31.16 mD to 6.81 mD. The permeability–saturation can be fitted as

$$k_h = 1758.4{S_h}^2 - 715.5S_h + 86.7 \; R^2 = 0.99 \quad (11)$$

$$k_v = 272.3{S_h}^2 - 173.2S_h + 31.1 \; R^2 = 0.99 \quad (12)$$

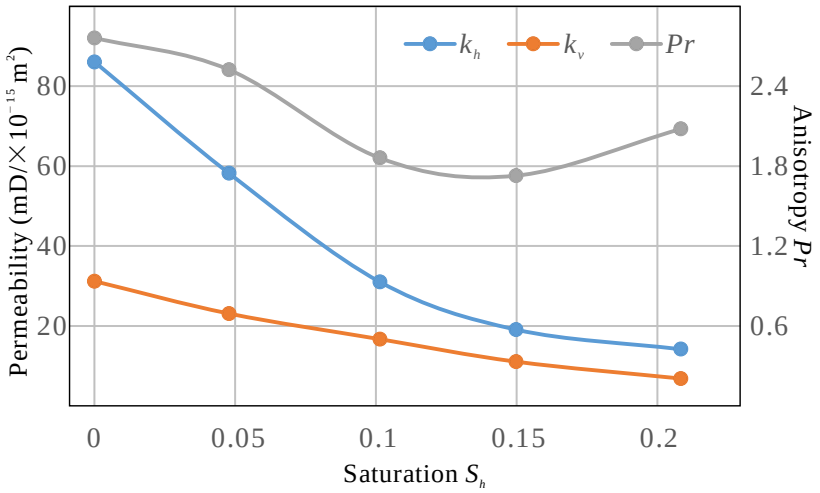



**Figure 8.** Permeability response for uniformly distributed hydrates.

Within the saturation range from 0 to 0.15, the reduction in horizontal permeability is larger than that of vertical permeability, resulting in a decrease in anisotropy ($Pr$ from 2.76 to 1.73). After reaching a saturation level of 0.2, the reduction in permeability decelerates and the anisotropy rebounds to 2.08. In general, the uniformly distributed hydrates may reduce the primary anisotropy induced by the bedding structure. With the saturation reduction in actual hydrate extraction engineering, the permeability anisotropy of the target reservoir may increase gradually.

#### 3.2.2. Effect of Preferentially Distributed Hydrates

For the preferentially distributed hydrates in a coarse layer, the permeability in both horizontal and vertical directions also decrease as the saturation increases (Figure 9). Specifically, the decrease in permeability in the horizontal direction is characterized by a piecewise pattern. The permeability undergoes a sharp decrease within the saturation range from 0 to 0.1 (from 86.06 mD to 19.56 mD), while the rate of reduction slows down within the saturation range from 0.1 to 0.2 (from 19.56 mD to 10.36 mD). The decrease in vertical permeability, on the other hand, exhibits a relatively minor magnitude (from 31.16 mD to 26.83 mD), and the relationship between permeability and saturation also adheres to a quadratic function as

$$k_v = 189.2{S_h}^2 - 186.4S_h + 32.6 \; R^2 = 0.98 \quad (13)$$

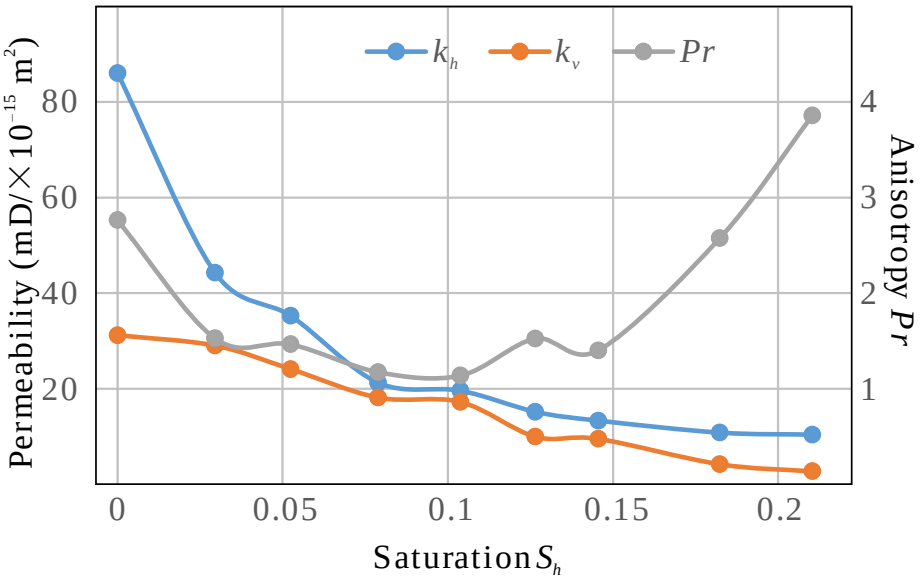



**Figure 9.** Permeability response for preferentially distributed hydrates in coarse layer.

As saturation increases, the change in anisotropy exhibits a U-shaped curve. The permeability anisotropy ratio $Pr$ decreases from 2.76 to 1.14 within the saturation range of 0–0.1, while it increases from 1.14 to 3.86 within the saturation range of 0.1–0.2. The permeability anisotropy ratio at the turning point, which has the minimum value throughout the entire evolution process, still remains greater than 1. Therefore, the principal directions of permeability have not changed and the horizontal permeability is always larger than the vertical permeability. Generally, the preferentially distributed hydrates may result in a down–up trend of permeability anisotropy.

## 4. Discussion

Permeability anisotropy and its evolution is an important basis for evaluating reservoir production potential. It is shown that the permeability of homogeneous sediments is isotropic. Moreover, the increase in hydrate saturation has minimal impact on isotropy, particularly within low saturation ranges ($S_h \leq 0.3$). At higher saturation levels, the blocking of most seepage channels will significantly increase the randomness of the simulation result, occasionally leading to an increase in anisotropy. In contrast, the permeability is anisotropic for layered sediments. The seepage process in layered sediments is primarily controlled by the dominant channels, which are formed by interconnected large-size pores in coarse layers. The dominant channels in coarse layers facilitate the horizontal flow while the fine layer blocks the vertical flow, thereby leading to the permeability anisotropy (Figure 10a,b).

According to the disturbance to the flow field, the hydrate effect on permeability mainly includes two modes: (1) Hydrates occupy the dominant channels, forming thrombotic blockages and causing a cross order decrease in flow velocity; (2) Hydrates occupy other locations, reducing the overall porosity, but have insignificant impact on the flow field (Figure 10c,d). For uniformly distributed hydrates, the probability of hydrate occurrence in different layers is consistent. However, the coarse layer exhibits a higher prevalence of dominant channels compared to the fine layer, resulting in more effective blockage within the coarse layer (Figure 10). Therefore, the number of effective dominant channels in the horizontal direction will decrease with increasing hydrate saturation, further resulting in a reduction in anisotropy.

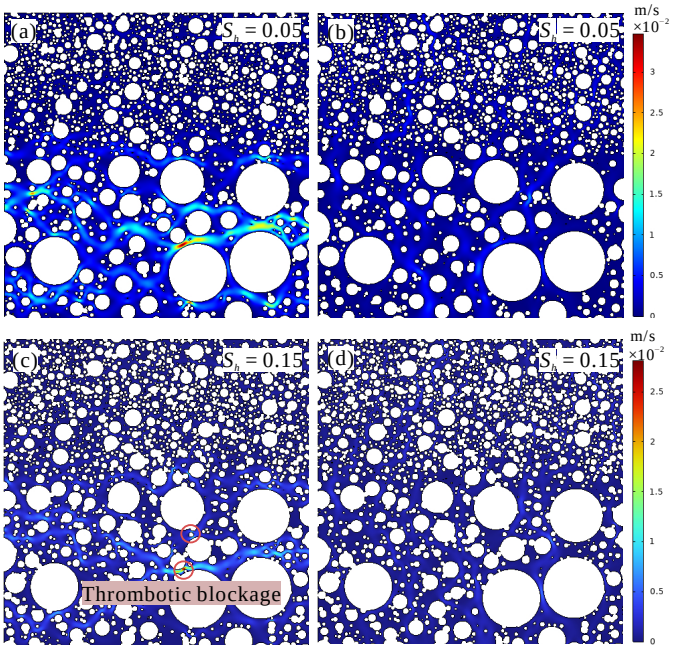



**Figure 10.** Effect of uniformly distributed hydrates on flow field: (**a**) $S_h$ = 0.05, horizontal flow; (**b**) $S_h$ = 0.05, vertical flow; (**c**) $S_h$ = 0.15, horizontal flow; and (**d**) $S_h$ = 0.15, vertical flow.

For preferentially distributed hydrates, the increase in saturation only influences the permeability of coarse layers. Theoretically, in the case of layered sediments, the overall horizontal permeability can be calculated by the weighted average of each individual layer's permeability, while the overall vertical permeability can be calculated by the harmonic average of each individual layer's permeability. Accordingly, the permeability anisotropy ratio of the two-layer model can be expressed as

$$Pr = (\frac{1}{2}k_c + \frac{1}{2}k_f)/(\frac{1}{2}{k_c}^{-1} + \frac{1}{2}{k_f}^{-1})^{-1} = \frac{(k_c + k_f)^2}{4k_c k_f} \quad (14)$$

where $k_c$ is the permeability of the coarse layer; $k_f$ is the permeability of fine layer.

The permeability of the fine layer remains unchanged because the presence of hydrates is limited to the coarse layer. Define $a$ as the ratio of permeability between coarse and fine layer:

$$k_f = ak_c \quad (15)$$

According to Equations (14) and (15), the permeability anisotropy can be expressed as

$$Pr = \frac{(1+a)^2}{4a} \quad (16)$$

The relationship between $Pr$ and $a$, as shown in Figure 11, can be divided into three stages:

(1) Low saturation stage: Part of the dominant channels is blocked, but the remaining channels still exhibit superior capacity compared to their vertical counterparts. The permeability of the coarse layer remains greater than that of the fine layer ($k_c > k_f$), making $a < 1$ (Figure 12a,b). As saturation increases, hydrate particles block more dominant channels, leading to a continuous decrease in the permeability of the coarse layer and a sharp decrease in permeability anisotropy (Figure 11).

(2) Medium saturation stage: With the increase in hydrate saturation, most of the dominant channels are blocked (Figure 12c,d). The permeability of the coarse layer approaches that of the fine layer ($k_c \approx k_f$). At this situation, a $\approx$ 1 and the layered

sediments can be regarded homogeneous permeable materials with the anisotropy ratio $Pr \approx 1$ (Figure 11).

(3) High saturation stage: Not only are the dominant channels blocked, but other minor seepage channels are also occupied by hydrates. The permeability of the coarse layer is even lower that of the fine layer ($k_c < k_f$, a > 1). At this situation, the fine layer becomes the concentrated area of horizontal dominant seepage, while the coarse layer acts as the barrier to block vertical flow (Figure 12c,d). As saturation increases, the lower permeability in the coarse layer will further enhance the blocking effect on vertical flow, thereby increasing the permeability anisotropy (Figure 11).

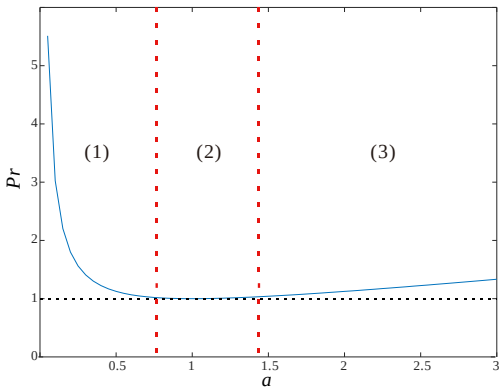



**Figure 11.** Relationship between permeability anisotropy $Pr$ and $a$.

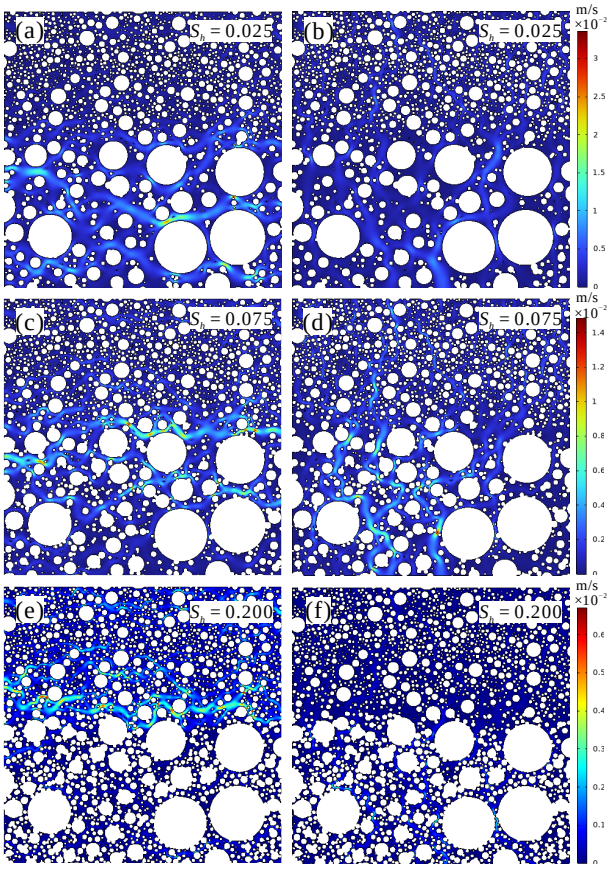



**Figure 12.** Effect of preferentially distributed hydrates on flow field: (**a**) $S_h$ = 0.025, horizontal flow; (**b**) $S_h$ = 0.025, vertical flow; (**c**) $S_h$ = 0.075, horizontal flow; (**d**) $S_h$ = 0.075, vertical flow; (**e**) $S_h$ = 0.200, horizontal flow; and (**f**) $S_h$ = 0.200, vertical flow.

Actually, the "dominant channel" is a relative concept. There will always be flow channels in porous media with higher flow velocity. After the coarse layer is blocked by hydrates, the dominant flow immediately turns to the unobstructed fine particle layer, still causing macroscopic anisotropy. Therefore, for a layered turbidite reservoir, permeability anisotropy will always affect the mass transport in the reservoir. In actual hydrate production, the decrease in hydrate saturation will lead to different change modes in permeability anisotropy. Specifically, for a "high-saturation" reservoir, the permeability anisotropy will initially decrease and subsequently increase during production, while for a "medium-saturation" or "low-saturation" reservoir, the permeability anisotropy will exhibit a consistently increasing trend with production.

## 5. Implication

During exploitation, permeability is one of the key parameters controlling production efficiency, reservoir stability and greenhouse gas sequestration. Limited by the experimental equipment and sample preparation technique, in current research, the directionality of permeability is usually ignored [23,61]. A few studies have observed the anisotropy of permeability in hydrate-bearing sediments, yet they mainly focused on the sample-scale anisotropy caused by the uneven distribution of hydrate, but overlooked the influence of primary sedimentary structures [44,50]. Naturally, NGH often occurs in unconsolidated sediments. Both the oriented particle arrangement in micro scale and the bedding structure in macro scale will cause the inherent anisotropy of permeability [21,62]. The most promising approach in practical engineering is the utilization of horizontal wells, which effectively mitigates the risk of hydrate secondary synthesis caused by excessive pressure differentials [63]. This method, in fact, benefits from the higher permeability in the horizontal direction. Nevertheless, with the change in the hydrate occurrence state, the permeability and anisotropy will change radically, which brings great uncertainty to the evaluation of engineering and environmental effects before NGH exploitation.

In this work, the turbidite sediment in Northern Cascadia is chosen as a typical case and the anisotropy caused by primary sedimentary structures is investigated. The blocking and "thrombus" effect of hydrate on the preponderance channels will lead to a nonlinear decline in permeability in this direction, which will reduce the control effect of the preponderance channel and further weaken the anisotropy of permeability. This suggests that the permeability anisotropy may increase with decreasing saturation during the reservoir production process, i.e., horizontal permeability becomes larger. Consequently, the efficiency of horizontal wells may be better than expected.

In the future, experimental tests will be the focus of our research. A permeability tensor testing system for unconsolidated sediment will be developed to test the permeability anisotropy of turbidite sediments. The test results will serve as validation for the simulation results of this work.

## 6. Conclusions

The presence of hydrates, as a crucial constituent of the solid framework, not only impacts overall permeability but also influences permeability anisotropy. A series of simulations are performed by integrating particle flow and computational fluid dynamics methods to construct the numerical samples and compute the evolution of permeability anisotropy. Based on the homogeneous and layered sediment models, the saturation sensitivity of permeability anisotropy is investigated and the following conclusions are obtained:

(1) The permeability is isotropic for homogeneous sediments while anisotropic for layered sediments in the absence of hydrates. The seepage process in layered sediments is primarily controlled by the dominant channels, which are formed by interconnected large-size pores in coarse layers. These dominant channels in coarse layers facilitate the horizontal flow while the fine layer blocks the vertical flow, thereby leading to the permeability anisotropy.

(2) A practical method for hydrate generation and saturation determination is developed, which allows for the representation of various pore habits. The permeability of homogeneous sediments decreases quadratically with the increase in hydrate saturation and the permeability isotropy remains unchanged with varying hydrate saturation, while the permeability anisotropy varies greatly with increasing hydrate saturation for layered sediments.
(3) For uniformly distributed hydrates, the more effective blockage in coarse layer than that in fine layer results in a reduction in anisotropy. While for preferentially distributed hydrates, the excess blocking of coarse layer makes the dominant channels transfer to the fine layer, further cause a U-shaped anisotropy–saturation curve characterized by a decrease–increase transformation.

**Author Contributions:** Conceptualization, R.L. and L.Z.; methodology, R.L. and Z.H.; software, R.L. and S.W.; validation, Z.H. and L.Z.; formal analysis, R.L. and J.Z.; investigation, Z.H. and J.Z.; resources, Z.H. and L.Z.; data curation, R.L. and S.W.; writing—original draft preparation, R.L.; writing—review and editing, Z.H. and L.Z.; visualization, R.L.; supervision, Z.H. and L.Z.; project administration, Z.H. and L.Z.; funding acquisition, Z.H., J.Z. and L.Z. All authors have read and agreed to the published version of the manuscript.

**Funding:** This research was funded by [the National Natural Science Foundation of China] grant number [52192623]; [the National Natural Science Foundation of China] grant number [42107190] and [the Key Research Program of the Institute of Geology & Geophysics, CAS] grant number [IGGCAS-201903].

**Institutional Review Board Statement:** Not applicable.

**Informed Consent Statement:** Not applicable.

**Data Availability Statement:** All relevant data are within the paper.

**Acknowledgments:** We would like to thank the editors and anonymous reviewers who have helped to improve the paper.

**Conflicts of Interest:** The authors declare no conflict of interest.

## References

1. Bahk, J.J.; Kim, D.H.; Chun, J.H.; Son, B.K.; Kim, J.H.; Ryu, B.J.; Torres, M.E.; Riedel, M.; Schultheiss, P. Gas hydrate occurrences and their relation to host sediment properties: Results from Second Ulleung Basin Gas Hydrate Drilling Expedition, East Sea. *Mar. Pet. Geol.* **2013**, *47*, 21–29. [CrossRef]
2. Biastoch, A.; Treude, T.; Rüpke, L.H.; Riebesell, U.; Roth, C.; Burwicz, E.B.; Park, W.; Latif, M.; Böning, C.W.; Madec, G.; et al. Rising Arctic Ocean temperatures cause gas hydrate destabilization and ocean acidification. *Geophys. Res. Lett.* **2011**, *38*, L08602. [CrossRef]
3. Boswell, R. Is Gas Hydrate Energy Within Reach? *Science* **2009**, *325*, 957–958. [CrossRef] [PubMed]
4. Boswell, R.; Collett, T.S. Current perspectives on gas hydrate resources. *Energy Environ. Sci.* **2011**, *4*, 1206–1215. [CrossRef]
5. Boswell, R.; Collett, T.S.; Frye, M.; Shedd, W.; McConnell, D.R.; Shelander, D. Subsurface gas hydrates in the northern Gulf of Mexico. *Mar. Pet. Geol.* **2012**, *34*, 4–30. [CrossRef]
6. Burton, Z.F.M.; Dafov, L.N. Testing the Sediment Organic Contents Required for Biogenic Gas Hydrate Formation: Insights from Synthetic 3-D Basin and Hydrocarbon System Modelling. *Fuels* **2022**, *3*, 555–562. [CrossRef]
7. Burton, Z.F.M.; Dafov, L.N. Salt Diapir-Driven Recycling of Gas Hydrate. *Geochem. Geophys. Geosystems* **2023**, *24*, e2022GC010704. [CrossRef]
8. Burton, Z.F.M.; Kroeger, K.F.; Hosford Scheirer, A.; Seol, Y.; Burgreen-Chan, B.; Graham, S.A. Tectonic Uplift Destabilizes Subsea Gas Hydrate: A Model Example From Hikurangi Margin, New Zealand. *Geophys. Res. Lett.* **2020**, *47*, e2020GL087150. [CrossRef]
9. Burton, Z.F.M.; McHargue, T.; Kremer, C.H.; Bloch, R.B.; Gooley, J.T.; Jaikla, C.; Harrington, J.; Graham, S.A. Peak Cenozoic warmth enabled deep-sea sand deposition. *Sci. Rep.* **2023**, *13*, 1276. [CrossRef]
10. Cai, J.C.; Xia, Y.X.; Lu, C.; Bian, H.; Zou, S.M. Creeping microstructure and fractal permeability model of natural gas hydrate reservoir. *Mar. Pet. Geol.* **2020**, *115*, 104282. [CrossRef]
11. Chong, Z.R.; Yang, S.H.B.; Babu, P.; Linga, P.; Li, X.S. Review of natural gas hydrates as an energy resource: Prospects and challenges. *Appl. Energy* **2016**, *162*, 1633–1652. [CrossRef]
12. Collett, T.S. Energy potential of natural gas hydrates. *AAPG Bull.* **2002**, *86*, 1971–1992.
13. Cundall, P.A.; Strack, O.D.L. A discrete numerical model for granular assemblies. *Géotechnique* **1979**, *29*, 47–65. [CrossRef]

14. Dai, S.; Kim, J.; Xu, Y.; Waite, W.F.; Jang, J.B.; Yoneda, J.; Collett, T.S.; Kumar, P. Permeability anisotropy and relative permeability in sediments from the National Gas Hydrate Program Expedition 02, offshore India. *Mar. Pet. Geol.* **2019**, *108*, 705–713. [CrossRef]
15. Dai, S.; Santamarina, J.C. Sampling disturbance in hydrate-bearing sediment pressure cores: NGHP-01 expedition, Krishna–Godavari Basin example. *Mar. Pet. Geol.* **2014**, *58*, 178–186. [CrossRef]
16. Deng, P.; Zhu, J.T. Anisotropy of Unsaturated Layered Soils: Impact of Layer Composition and Domain Size. *Soil Sci. Soc. Am. J.* **2015**, *79*, 487–494. [CrossRef]
17. Ding, Y.; Qian, A.; Lu, H. Applications of the Discrete Element Method for Gas Hydrate-Bearing Sediments: Recent Advances and Perspectives. *Energy Fuels* **2022**, *36*, 10766–10784. [CrossRef]
18. Ding, Y.; Qian, A.; Lu, H. Three-dimensional discrete element modeling of the shear behavior of cemented hydrate-bearing sands. *J. Nat. Gas Sci. Eng.* **2022**, *101*, 104526. [CrossRef]
19. Feng, Y.; Chen, L.; Suzuki, A.; Kogawa, T.; Okajima, J.; Komiya, A.; Maruyama, S. Numerical analysis of gas production from reservoir-scale methane hydrate by depressurization with a horizontal well: The effect of permeability anisotropy. *Mar. Pet. Geol.* **2019**, *102*, 817–828. [CrossRef]
20. Feng, Y.C.; Chen, L.; Suzuki, A.; Kogawa, T.; Okajima, J.; Komiya, A.; Maruyama, S. Numerical analysis of gas production from layered methane hydrate reservoirs by depressurization. *Energy* **2019**, *166*, 1106–1119. [CrossRef]
21. Garcia, X.; Akanji, L.T.; Blunt, M.J.; Matthai, S.K.; Latham, J.P. Numerical study of the effects of particle shape and polydispersity on permeability. *Phys. Rev. E* **2009**, *80*, 1. [CrossRef] [PubMed]
22. Han, Z.; Zhang, L.; Zhou, J.; Pan, Z.; Wang, S.; Li, R. Effects of hydrate occurring mechanisms and saturation on the mechanical properties of hydrate-bearing sediments: Numerical study based on simplified DEM simulation. *J. Nat. Gas Sci. Eng.* **2022**, *108*, 104804. [CrossRef]
23. Hu, C.; Jia, Y.; Duan, Z. The influence of inhomogeneous hydrate formation on permeability anisotropy of porous media. *Geo-Mar. Lett.* **2021**, *41*, 10. [CrossRef]
24. Hu, C.; Liu, X.; Jia, Y.; Duan, Z. Permeability anisotropy of methane hydrate-bearing sands: Insights from CT scanning and pore network modelling. *Comput. Geotech.* **2020**, *123*, 103568. [CrossRef]
25. Jiang, M.J.; Konrad, J.M.; Leroueil, S. An efficient technique for generating homogeneous specimens for DEM studies. *Comput. Geotech.* **2003**, *30*, 579–597. [CrossRef]
26. Jin, G.; Torres-Verdin, C.; Lan, C. Pore-Level Study of Grain-Shape Effects on Petrophysical Properties of Porous Media. In Proceedings of the SPWLA 50th Annual Logging Symposium, The Woodlands, TX, USA, 21–24 June 2009; p. SPWLA–2009-62136.
27. Katagiri, J.; Konno, Y.; Yoneda, J.; Tenma, N. Pore-scale modeling of flow in particle packs containing grain-coating and pore-filling hydrates: Verification of a Kozeny–Carman-based permeability reduction model. *J. Nat. Gas Sci. Eng.* **2017**, *45*, 537–551. [CrossRef]
28. Kim, B.; Zhang, Y.G. Methane hydrate dissociation across the Oligocene-Miocene boundary. *Nat. Geosci.* **2022**, *15*, 203–209. [CrossRef]
29. Kimura, S.; Ito, T.; Noda, S.; Kaneko, H.; Suzuki, K.; Yasuda, H.; Minagawa, H. Water Permeability Evolution With Faulting for Unconsolidated Turbidite Sand in a Gas-Hydrate Reservoir in the Eastern Nankai Trough Area of Japan. *J. Geophys. Res.: Solid Earth* **2019**, *124*, 13415–13426. [CrossRef]
30. Kleinberg, R.L.; Flaum, C.; Griffin, D.D.; Brewer, P.G.; Malby, G.E.; Peltzer, E.T.; Yesinowski, J.P. Deep sea NMR: Methane hydrate growth habit in porous media and its relationship to hydraulic permeability, deposit accumulation, and submarine slope stability. *J. Geophys. Res. Solid Earth* **2003**, *108*, 1. [CrossRef]
31. Konno, Y.; Masuda, Y.; Hariguchi, Y.; Kurihara, M.; Ouchi, H. Key Factors for Depressurization-Induced Gas Production from Oceanic Methane Hydrates. *Energy Fuels* **2010**, *24*, 1736–1744. [CrossRef]
32. Kumar, A.; Maini, B.; Bishnoi, P.R.; Clarke, M.; Zatsepina, O.; Srinivasan, S. Experimental determination of permeability in the presence of hydrates and its effect on the dissociation characteristics of gas hydrates in porous media. *J. Pet. Sci. Eng.* **2010**, *70*, 114–122. [CrossRef]
33. Kvenvolden, K.A. Methane hydrate—A major reservoir of carbon in the shallow geosphere? *Chem. Geol.* **1988**, *71*, 41–51. [CrossRef]
34. Kvenvolden, K.A. Methane hydrate in the global organic carbon cycle. *Terra Nova* **2002**, *14*, 302–306. [CrossRef]
35. Lagioia, R.; Sanzeni, A.; Colleselli, F. Air, water and vacuum pluviation of sand specimens for the triaxial apparatus. *Soils Found* **2006**, *46*, 61–67. [CrossRef]
36. Lei, L.; Seol, Y.; Choi, J.-H.; Kneafsey, T.J. Pore habit of methane hydrate and its evolution in sediment matrix–Laboratory visualization with phase-contrast micro-CT. *Mar. Pet. Geol.* **2019**, *104*, 451–467. [CrossRef]
37. Li, R.; Zhang, L.; Han, Z.; Zhou, J.; Wang, S.; Schüttrumpf, H. Effect of interlayer mixed zone and effective stress on permeability anisotropy of NGH turbidite reservoir. *Energy* **2023**, *284*, 129172. [CrossRef]
38. Li, R.; Zhang, L.; Zhou, J.; Han, Z.; Pan, Z.; Schüttrumpf, H. Investigation on permeability anisotropy in unconsolidated hydrate-bearing sediments based on pore-scale numerical simulation: Effect of mineral particle shape and pore-filling. *Energy* **2023**, *267*, 126456. [CrossRef]
39. Liu, W.; Wu, Z.; Li, J.; Zheng, J.; Li, Y. The seepage characteristics of methane hydrate-bearing clayey sediments under various pressure gradients. *Energy* **2020**, *191*, 116507. [CrossRef]
40. Lowe, D. Sediment Gravity Flows: II Depositional Models with Special Reference to the Deposits of High-Density Turbidity Currents. *J. Sediment. Res.* **1982**, *52*, 279–297.

41. Lu, H.L.; Kawasaki, T.; Ukita, T.; Moudrakovski, I.; Fujii, T.; Noguchi, S.; Shimada, T.; Nakamizu, M.; Ripmeester, J.; Ratcliffe, C. Particle size effect on the saturation of methane hydrate in sediments-Constrained from experimental results. *Mar. Pet. Geol.* **2011**, *28*, 1801–1805. [CrossRef]
42. Lu, H.L.; Seo, Y.T.; Lee, J.W.; Moudrakovski, I.; Ripmeester, J.A.; Chapman, N.R.; Coffin, R.B.; Gardner, G.; Pohlman, J. Complex gas hydrate from the Cascadia margin. *Nature* **2007**, *445*, 303–306. [CrossRef] [PubMed]
43. Makogon, Y.F. Natural gas hydrates—A promising source of energy. *J. Nat. Gas Sci. Eng.* **2010**, *2*, 49–59. [CrossRef]
44. Mao, P.X.; Sun, J.X.; Ning, F.L.; Hu, G.W.; Wan, Y.Z.; Cao, X.X.; Wu, N.Y. Effect of permeability anisotropy on depressurization-induced gas production from hydrate reservoirs in the South China Sea. *Energy Sci. Eng.* **2020**, *8*, 2690–2707. [CrossRef]
45. Masuda, Y.; Naganawa, S.; Ando, S.; Sato, K. Numerical calculation of gas production performance from reservoirs containing natural gas hydrates. *SPE J.* **1997**, *29*, 38291.
46. Moernaut, J.; Van Daele, M.; Strasser, M.; Clare, M.A.; Heirman, K.; Viel, M.; Cardenas, J.; Kilian, R.; de Guevara, B.L.; Pino, M.; et al. Lacustrine turbidites produced by surficial slope sediment remobilization: A mechanism for continuous and sensitive turbidite paleoseismic records. *Mar. Geol.* **2017**, *384*, 159–176. [CrossRef]
47. Mutti, E. Turbidite Systems and Their Relations to Depositional Sequences. In *Provenance of Arenites*; Zuffa, G.G., Ed.; Springer: Dordrecht, The Netherlands, 1985; pp. 65–93.
48. Ren, X.; Guo, Z.; Ning, F.; Ma, S. Permeability of hydrate-bearing sediments. *Earth Sci. Rev.* **2020**, *202*, 103100. [CrossRef]
49. Ruppel, C. Permafrost-Associated Gas Hydrate: Is It Really Approximately 1% of the Global System? *J. Chem. Eng. Data* **2015**, *60*, 429–436. [CrossRef]
50. Ruppel, C.D.; Kessler, J.D. The interaction of climate change and methane hydrates. *Rev. Geophys.* **2017**, *55*, 126–168. [CrossRef]
51. Shanmugam, G. Ten turbidite myths. *Earth-Sci. Rev.* **2002**, *58*, 311–341. [CrossRef]
52. Shi, J.; Haegeman, W.; Cnudde, V. Anisotropic small-strain stiffness of calcareous sand affected by sample preparation, particle characteristic and gradation. *Géotechnique* **2021**, *71*, 305–319. [CrossRef]
53. Sloan, E.D. Fundamental principles and applications of natural gas hydrates. *Nature* **2003**, *426*, 353–359. [CrossRef] [PubMed]
54. Sloan, E.D.; Koh, C.A. *Clathrate Hydrates of Natural Gases*; CRC Press: Boca Raton, FL, USA, 2007.
55. Torres, M.E.; Trehu, A.M.; Cespedes, N.; Kastner, M.; Wortmann, U.G.; Kim, J.H.; Long, P.; Malinverno, A.; Pohlman, J.W.; Riedel, M.; et al. Methane hydrate formation in turbidite sediments of northern Cascadia, IODP Expedition 311. *Earth Planet. Sci. Lett.* **2008**, *271*, 170–180. [CrossRef]
56. Wang, J.; Zhang, L.; Ge, K.; Zhao, J.; Song, Y. Characterizing anisotropy changes in the permeability of hydrate sediment. *Energy* **2020**, *205*, 117997. [CrossRef]
57. Wang, L.; Li, Y.; Wu, P.; Shen, S.; Liu, T.; Leng, S.; Chang, Y.; Zhao, J. Physical and mechanical properties of the overburden layer on gas hydrate-bearing sediments of the South China sea. *J. Pet. Sci. Eng.* **2020**, *189*, 107020. [CrossRef]
58. Ye, J.-L.; Qin, X.-W.; Xie, W.-W.; Lu, H.-L.; Ma, B.-J.; Qiu, H.-J.; Liang, J.-Q.; Lu, J.-A.; Kuang, Z.-G.; Lu, C.; et al. The second natural gas hydrate production test in the South China Sea. *China Geol.* **2020**, *3*, 197–209. [CrossRef]
59. Yoneda, J.; Oshima, M.; Kida, M.; Kato, A.; Konno, Y.; Jin, Y.; Jang, J.B.; Waite, W.F.; Kumar, P.; Tenma, N. Permeability variation and anisotropy of gas hydrate-bearing pressure-core sediments recovered from the Krishna-Godavari Basin, offshore India. *Mar. Pet. Geol.* **2019**, *108*, 524–536. [CrossRef]
60. Yoo, D.G.; Kang, N.K.; Yi, B.Y.; Kim, G.Y.; Ryu, B.J.; Lee, K.; Lee, G.H.; Riedel, M. Occurrence and seismic characteristics of gas hydrate in the Ulleung Basin, East Sea. *Mar. Pet. Geol.* **2013**, *47*, 236–247. [CrossRef]
61. You, Z.; Li, Y.; Yang, M.; Wu, P.; Liu, T.; Li, J.; Hu, W.; Song, Y. Investigation of particle-scale mechanical behavior of hydrate-bearing sands using DEM: Focus on hydrate habits. *Energy* **2024**, *289*, 130088.
62. Zavala, C.; Arcuri, M. Intrabasinal and extrabasinal turbidites: Origin and distinctive characteristics. *Sediment. Geol.* **2016**, *337*, 36–54. [CrossRef]
63. Zhou, M.; Soga, K.; Xu, E.; Uchida, S.; Yamamoto, K. Numerical study on Eastern Nankai Trough gas hydrate production test. In Proceedings of the Offshore Technology Conference, Houston, TX, USA, 5–8 May 2014; p. D041S055R003.


**Disclaimer/Publisher's Note:** The statements, opinions and data contained in all publications are solely those of the individual author(s) and contributor(s) and not of MDPI and/or the editor(s). MDPI and/or the editor(s) disclaim responsibility for any injury to people or property resulting from any ideas, methods, instructions or products referred to in the content.